Supplementary information: Microwave-based quantum control and coherence protection of tin-vacancy spin qubits in a strain-tuned diamond membrane heterostructure

Xinghan Guo[1,*], Alexander M. Stramma[2,*], Zixi Li[1], William G. Roth[2], Benchen Huang[3], Yu Jin[3], Ryan A. Parker[2], Jesús Arjona Martínez[2], Noah Shofer[2], Cathryn P. Michaels[2], Carola P. Purser[2], Martin H. Appel[2], Evgeny M. Alexeev[2,4], Tianle Liu[5], Andrea C. Ferrari[4], David D. Awschalom[1,5,6], Nazar Delegan[1,6], Benjamin Pingault[6,7], Giulia Galli[1,3,6], F. Joseph Heremans[1,6], Mete Atatüre[2,†], and Alexander A. High[1,6,†]

[1] *Pritzker School of Molecular Engineering, University of Chicago, Chicago, IL 60637, USA*
[2] *Cavendish Laboratory, University of Cambridge, Cambridge CB3 0HE, United Kingdom*
[3] *Department of Chemistry, University of Chicago, Chicago, IL 60637, USA*
[4] *Cambridge Graphene Centre, University of Cambridge,Cambridge CB3 0FA, United Kingdom*
[5] *Department of Physics, University of Chicago, Chicago, IL 60637, USA*
[6] *Center for Molecular Engineering and Materials Science Division, Argonne National Laboratory, Lemont, IL 60439, USA and*
[7] *QuTech, Delft University of Technology, 2600 GA Delft, The Netherlands*

CONTENTS

I. TIN VACANCY CENTER (SnV^-) IN STRAINED DIAMOND MEMBRANES

A. Hamiltonian of the strained SnV^-

The SnV^- center is a spin-1/2 system. In a mean-field orbital picture, the system has three electrons in four spin orbitals ($\{|e_x\uparrow\rangle, |e_x\downarrow\rangle, |e_y\uparrow\rangle, |e_y\downarrow\rangle\}$). Both its electronic ground and excited states are doubly-degenerate; the degeneracy may be lifted by applying strain and/or by spin-orbit interaction. We write the spin Hamiltonian of the system in the minimum model of 4 electrons and 3 orbitals, for the ground (g) and excited (u) state $H_{g,u}$, as the sum of four terms: spin-orbit (SO) interaction ($\hat{H}_{\rm SO}$); electron-phonon interaction due to the Jahn-Teller effect; strain field, and interaction with an external, static magnetic field B (Zeeman effect, $\hat{H}_Z$). Following Ref [1], we write the term arising from Jahn-Teller distortions in the same form as that describing the strain interaction. Below we merge the two terms into one, that for simplicity we call $\hat{H}_{\rm strain}$. Hence the Hamiltonian is written as:

$$\hat{H}_{\rm sys} = \hat{H}_{\rm SO} + \hat{H}_{\rm strain} + \hat{H}_Z. \tag{1}$$

In the following three subsections, we discuss each term of the Hamiltonian.

1. Spin-orbit coupling

The component of the orbital angular momentum operator $\hat{L}_x, \hat{L}_y$ vanish for the Hamiltonian expressed in the $\{|e_x\rangle, |e_y\rangle\}$ basis [1] and only the following term is non-zero:

$$\hat{L}_z = \begin{bmatrix} 0 & -i \\ i & 0 \end{bmatrix}, \tag{2}$$

where we have set $\hbar$ to 1. Therefore, using the $\{|e_x\uparrow\rangle, |e_x\downarrow\rangle, |e_y\uparrow\rangle, |e_y\downarrow\rangle\}$ basis, the SO Hamiltonian can be represented as:

$$\hat{H}_{SO} = \lambda \hat{L}_z \hat{S}_z = \frac{\lambda}{2} \begin{bmatrix} 0 & -i \\ i & 0 \end{bmatrix} \otimes \begin{bmatrix} 1 & 0 \\ 0 & -1 \end{bmatrix} = \begin{bmatrix} 0 & 0 & -i\lambda/2 & 0 \\ 0 & 0 & 0 & i\lambda/2 \\ i\lambda/2 & 0 & 0 & 0 \\ 0 & -i\lambda/2 & 0 & 0 \end{bmatrix}. \tag{3}$$

2. Strain field

The term of the Hamiltonian representing the presence of a strain field can be written as:

$$\hat{H}_{\rm strain} = \begin{bmatrix} \varepsilon_{A_1} - \varepsilon_{E_x} & \varepsilon_{E_y} \\ \varepsilon_{E_y} & \varepsilon_{A_1} + \varepsilon_{E_x} \end{bmatrix} \otimes \mathbb{I}_2. \tag{4}$$

The elements $\{\varepsilon_{A_1}, \varepsilon_{E_x}, \varepsilon_{E_y}\}$ represent the energy response induced by strain belonging to the different irreducible representations A_1, E_x, E_y of the D_{3d} point group of the defect, and are expressed in the SnV^- center's local frame, where the z-axis corresponds to the high symmetry axis of the SnV which is the quantization axis. For example, $\varepsilon_{A_1} = \langle\Psi|(H - H_0)|\Psi|\Psi|(H - H_0)|\Psi\rangle$, where H_0 is the electronic Hamiltonian in the absence of strain and H is the electronic Hamiltonian, which includes the strain field applied to the supercell by changing the lattice parameters. Here $|\Psi\rangle$ represents a Slater determinant expressed in the $\{|e_x\uparrow\rangle, |e_x\downarrow\rangle, |e_y\uparrow\rangle, |e_y\downarrow\rangle\}$ basis.

We can write each term of Eq. 4 as a linear combination of the components of the strain tensor (ϵ):

$$\begin{aligned} \varepsilon_{A_1} &= t_\perp (\epsilon_{xx} + \epsilon_{yy}) + t_\parallel \epsilon_{zz}, \\ \varepsilon_{E_x} &= d (\epsilon_{xx} - \epsilon_{yy}) + f \epsilon_{zx}, \\ \varepsilon_{E_y} &= -2d \epsilon_{xy} + f \epsilon_{yz}, \end{aligned} \tag{5}$$

where $\epsilon_{xx}, \epsilon_{yy}, \epsilon_{zz}$ represent the diagonal components of the strain tensor in the x, y, z directions and $\epsilon_{xy}, \epsilon_{yz}, \epsilon_{zx}$ represent the shear strain components; $t_\perp, t_\parallel, d$, and f are partial derivatives written as $\frac{\partial \varepsilon_{A_1}}{\partial(\epsilon_{xx}+\epsilon_{yy})}$, $\frac{\partial \varepsilon_{A_1}}{\partial \epsilon_{zz}}$, $\frac{\partial \varepsilon_{E_x}}{\partial(\epsilon_{xx}-\epsilon_{yy})}$, $\frac{\partial \varepsilon_{E_x}}{\partial \epsilon_{zx}}$,

respectively. These four strain-susceptibility parameters completely describe the strain-response of the ground and excited electronic states. In the following, we ignore the diagonal term ϵ_{A_1}, which amounts to a global emission wavelength shift. Hence, the strain Hamiltonian has the following form:

$$\hat{H}_{\text{strain}} = \begin{bmatrix} -\varepsilon_{E_x} & \varepsilon_{E_y} \\ \varepsilon_{E_y} & \varepsilon_{E_x} \end{bmatrix} \otimes \mathbb{I}_2 = \begin{bmatrix} -\varepsilon_{E_x} & 0 & \varepsilon_{E_y} & 0 \\ 0 & -\varepsilon_{E_x} & 0 & \varepsilon_{E_y} \\ \varepsilon_{E_y} & 0 & \varepsilon_{E_x} & 0 \\ 0 & \varepsilon_{E_y} & 0 & \varepsilon_{E_x} \end{bmatrix}. \tag{6}$$

3. Zeeman effect

Due to the D_{3d} symmetry of the defect, the orbital component $H_{Z,L}$ of the Hamiltonian H_Z only includes a term $\hat{L}_z B_z$ [1], with a pre-factor q [2], called in the literature *effective reduction factor*, accounting for: (i) electron-phonon interaction (so-called Ham term), and (ii) the symmetry of the defect being lower than $O(3)$ (so-called Steven's factor). Note that both terms have different values for the ground and excited states and hence the q parameter is different in the ground and excited states. The H_Z Hamiltonian is written as the sum of an orbital $H_{Z,L}$ and spin component $H_{Z,S}$

$$\hat{H}_Z = \hat{H}_{Z,L} + \hat{H}_{Z,S} = q\mu_B\gamma_L\hat{L}_z B_z + g\mu_B\hat{\mathbf{S}}\cdot\mathbf{B} - 2\mu_B\delta_f\hat{S}_z B_z, \tag{7}$$

where μ_B is the Bohr magneton and B_x, B_y, B_z are the components of the external, static magnetic field along the crystal frame x, y, z directions, respectively. The last term on the right hand side of Eq. 7 originates from correcting with a factor δ the electronic Landé g factor to account for spin-phonon interaction mediated by spin-orbit coupling [2]. For all the experimental interpretations, we'll only use the Ham factor and set the Steven's factor as 1 except section IV A where we gave estimates on the possible values of Steven's factor.

B. Strain susceptibility

In the presence of a strain field, the degeneracy of the ground (gs) and excited (es) states is lifted and we call $\triangle_{\text{gs(es)}}$ the energy difference between the two states split by the degeneracy. By diagonalizing the strain Hamiltonian defined in Eq. 6, we obtain:

$$\triangle_{\text{gs(es)}} = 2\sqrt{[d_{\text{gs(es)}}(\epsilon_{xx} - \epsilon_{yy}) + f_{\text{gs(es)}}\epsilon_{zx}]^2 + [-2d_{\text{gs(es)}}\epsilon_{xy} + f_{\text{gs(es)}}\epsilon_{yz}]^2}, \tag{8}$$

where the strain-susceptibilities are computed from density functional theory (DFT) calculations. We performed DFT calculations employing both the PBE [3] and SCAN [4] functionals, and a 511-atom supercell with a [0.5, 0.5] occupation number for the $|e_x\downarrow\rangle, |e_y\downarrow\rangle$ orbitals. We approximated the splittings by the energy difference of the corresponding Kohn-Sham (KS) orbitals. The strain susceptibilities $d_{\text{gs}}, d_{\text{es}}, f_{\text{gs}}, f_{\text{es}}$ can be obtained from Eq. 8 by varying the lattice parameters of the supercell to generate $(\epsilon_{xx} - \epsilon_{yy})$ and ϵ_{zx} strain, respectively. Our results are summarized in Table. S1. Note the similarity of results obtained with the two different functionals.

Functional	d_{gs}	d_{es}	f_{gs}	f_{es}
PBE	0.787	0.956	-0.562	-2.555
SCAN	0.834	0.921	-0.563	-2.592

TABLE S1. Computed strain susceptibilities (see text) of the SnV^- defect in diamond, in units of PHz/strain, obtained with the PBE and SCAN functionals.

C. Strain magnitude simulation

We use COMSOL to simulate the strain profile of the suspended area measured in experiments. Since the strain expression ϵ in section I A is defined in local SnV frame while the simulation result $\tilde{\epsilon}$ returns to the lab frame, a combination of rotation matrices are applied. From $\langle 100|100\rangle$ to $\langle 110|110\rangle$ to $\langle 111|111\rangle$, the rotation operators are $\hat{R}_z(45°)$ and $\hat{R}_y(54.7°)$, respectively:

$$\epsilon = \hat{R}_y^\dagger(54.7°)\ \hat{R}_z^\dagger(45°)\ \tilde{\epsilon}\ \hat{R}_z(45°)\ \hat{R}_y(54.7°) \tag{9}$$

Here $\hat{R}_y(\theta)$ and $\hat{R}_z(\theta)$ refer to:

$$\hat{R}_y(\theta) = \begin{bmatrix} \cos(\theta) & 0 & \sin(\theta) \\ 0 & 1 & 0 \\ -\sin(\theta) & 0 & \cos(\theta) \end{bmatrix}, \qquad \hat{R}_z(\theta) = \begin{bmatrix} \cos(\theta) & -\sin(\theta) & 0 \\ \sin(\theta) & \cos(\theta) & 0 \\ 0 & 0 & 1 \end{bmatrix} \tag{10}$$

In COMSOL simulation, we use the actual three dimensional (3D) geometry for the diamond membrane and the trench. The temperature-dependent thermal expansion ratio for diamond and fused silica are obtained from these references:[5–8]. The initial strain-free temperature is set to 450 °C which is the HSQ healing temperature [9], while the final temperature is set to 4 K. We note that thermal expansion ratios for both fused silica and diamond become negligible below 30 K, thus the simulated strain profile is nearly constant within the temperature range of interest (1.7 K to 7 K) in this study. The simulated structure and the strain distributions of E_{xx} and E_{yy} are shown in Figure S1. Since the off-diagonal shear strain is 2-3 orders of magnitude smaller than the diagonal tensile strain, we use the following matrix to represent the simulated strain value:

$$\tilde{\epsilon} = \begin{bmatrix} 1.3e^{-3} & 0 & 0 \\ 0 & 6.8e^{-4} & 0 \\ 0 & 0 & -2.5e^{-4} \end{bmatrix}, \qquad \epsilon = \begin{bmatrix} 1.6e^{-4} & -1.8e^{-4} & 5.8e^{-4} \\ -1.8e^{-4} & 9.9e^{-4} & -2.5e^{-4} \\ 5.8e^{-4} & -2.5e^{-4} & 5.8e^{-4} \end{bmatrix} \tag{11}$$

We note that although $\tilde{\epsilon}$ only includes diagonal elements, the transformed strain tensor ϵ in SnV local frame contains non-negligible off-diagonal elements which could affect the properties of the SnV center through both d and f parameters. By comparing the simulated branch splitting value using equation 8 and PBE results with the actual experimental values, we observed the actual strain to be 0.55 times the simulated value, as shown in Figure S1 (d). This magnitude mismatch could come from either the approximation of energy splittings from KS orbitals being inaccurate, the mismatch of the thermal expansion ratios between COMSOL simulation and reality, or an even lower softening temperature of HSQ rather than the healing temperature [9]. More comprehensive studies of the energy response to strain would require a higher level of method, e.g., embedding theory [10], which we left for future investigations. In the following calculations, we add this 0.55 pre-factor to the simulated strain tensor to best capture the system properties.

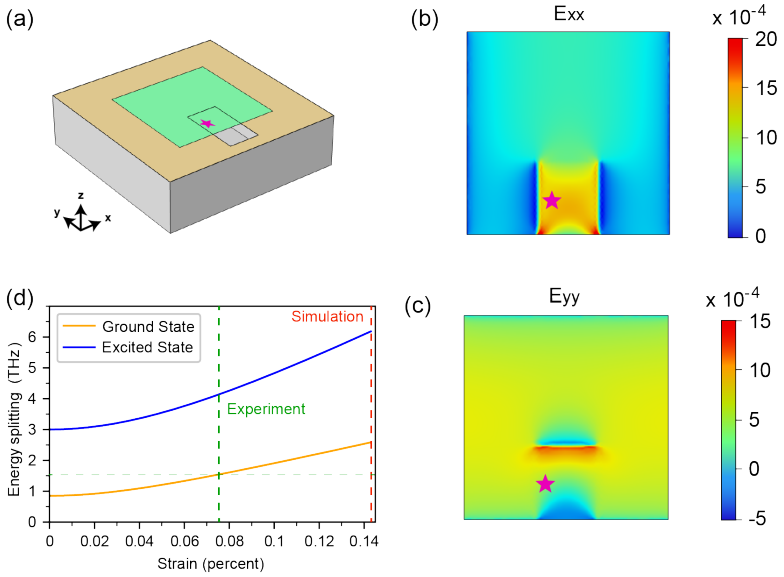

FIG. S1. Strain profile of the diamond membrane. (a) The 3D structure of the simulated device. The total length of the carrier wafer is limited to 350 um. (b-c) The E_{xx} (E_{yy}) strain profile on the membrane. The position of the SnV center characterized in the main text and SI is labelled as a red star. (d) The energy splitting between two orbital branches in ground and excited states. The simulated strain and the experimentally observed strain magnitudes are labelled in dashed red and green lines, respectively.

D. Strain magnitude discussion

We qualitatively categorize the strain magnitude to different regimes via the ground state energy splitting Δ_{gs}. In the spin-orbit regime, this energy splitting is nearly constant, while the splitting is linear with the external strain when in high-strain regime. Guided by that, we use $\Delta_{gs} = 1200\,\mathrm{GHz}$ as the boundary between the spin-orbit regime and the intermediate regime, and $\Delta_{gs} = 2600\,\mathrm{GHz}$ to identify intermediate and high strain regime. For our work, those values corresponding to strain magnitudes of 0.055 % and 0.143 %. Here to plot the optical transitions, the magnetic field is set to 80 mT along the quantization axis ($\langle 111|111\rangle$ direction) and the strain profile is set to be the same as COMSOL simulated profile but with an additional scaling factor. The calculated relative energy difference of the four $\{A1, A2, B1, B2\}$ transitions are plotted in Figure S2. Compared with the defined low strain "spin-orbit" regime and the high strain regime, our experimentally observed result sits in between, indicating a non-trivial intermediate region where neither spin-orbit coupling or strain shall we treated as perturbation terms. We note that unlike SiV centers [11], SnV obtains different quenching q factors at ground (0.471) and excited states (0.125) [2], leading to a non-zero splitting between spin-conserving transitions. We also extrapolate a qubit frequency ω_s of 2.1 GHz which is lower than the ODMR frequency reported in the main text (2.755 GHz). This mismatch could originate from the slight difference between the displayed and the real magnetic field due to hysteresis and the deviation of the effective reduction factors under strain from that in Ref [2].

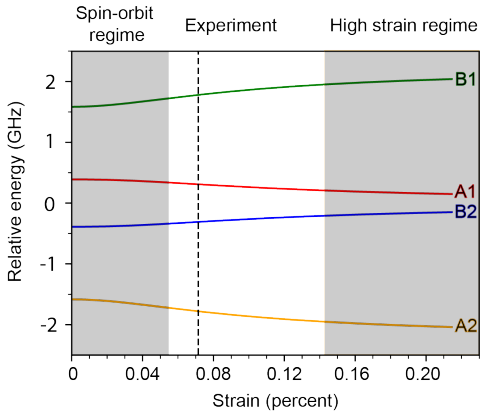

FIG. S2. Spin-conserving transition frequencies with respect to different strain magnitudes. The relative strain profile stays the same with only the scaling factor sweeping. The magnitude of the strain is defined by the norm of the tensor. The B field is set to be 80 mT along the quantization axis $\langle 111|111\rangle$ which is in line with the experimental configuration.

II. MW CONTROL OF THE SNV

A. MW magnetic response

At zero strain, the SnV spin qubit cannot be manipulated by microwave due to different orbits associated with the spin level. As stated in [11], the presence of the crystal strain introduces orbit superposition to SnV's spin qubit eigenstates, allowing for the coherent control of SnV via external microwave field with qubit frequency ω_s. Here we use the electronic g factor to characterize the ability of the MW field (AC B filed) to the spin state of the SnV, including both spin and orbit response of the external magnetic field:

$$g = \frac{2}{\mu_B} \langle e1\downarrow| \left(\hat{H}^{ac}_{Z,L} + \hat{H}^{ac}_{Z,S}\right) |e2\uparrow\rangle \tag{12}$$

$$\hat{H}^{ac}_{Z,L} + \hat{H}^{ac}_{Z,S} = \begin{bmatrix} B^{ac}_z & B^{ac}_x - iB^{ac}_y & -iqB^{ac}_z & 0 \\ B^{ac}_x + iB^{ac}_y & -B^{ac}_z & 0 & -iqB^{ac}_z \\ iqB^{ac}_z & 0 & B^{ac}_z & B^{ac}_x - iB^{ac}_y \\ 0 & iqB^{ac}_z & B^{ac}_x + iB^{ac}_y & -B^{ac}_z \end{bmatrix} \tag{13}$$

Here the $\mathbf{B}^{ac}$ is a vector with unitary length indicating the direction of the oscillating B field of the microwave. The $\langle e1\downarrow|$ and $|e2\uparrow\rangle$ are the two spin states of the SnV under external, static B field. The Ham reduction factor q of the

ground state is set to 0.471 according to [2]. First we investigate the effect of strain magnitude to the transverse and longitudinal g factor. The result is shown in Figure S3 (a), indicating a g factor of 1.64. Here the static **B** field set to be 80 mT along the quantization axis, which is in line with our experimental setup. We then investigate the angular dependence of the transverse g factor with different static field orientations using our experimentally observed strain profile. We note that the g factor has a weak angular dependence, indicating a consistently efficient MW driving efficiency regardless of the static B field orientation, highlighting the robustness of the strained SnV centers.

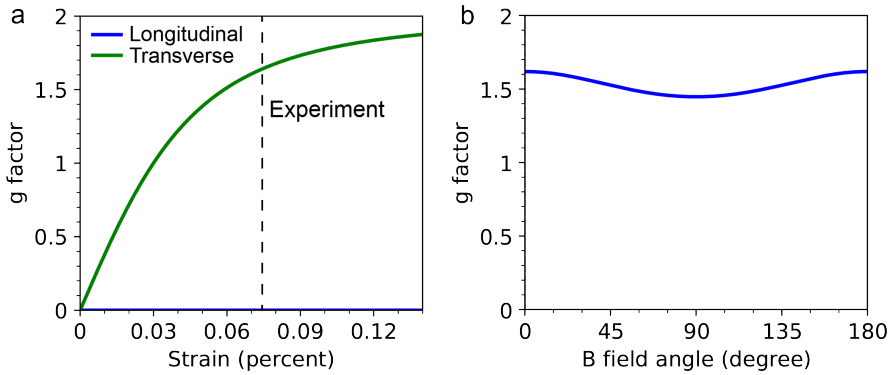

FIG. S3. MW g factor calculation. (a) The transverse and longitudinal g factor with respect to the strain magnitude. (b) The angular dependence of the g factor. The static B field is set to be 80 mT along the quantization axis $\langle 111|111\rangle$.

B. Device info

In this work we utilized on-chip coplanar waveguide (CPW) to deliver microwave signals to target SnV centers. Compared with wire-bonded metal striplines [12], lithography-defined CPW offers deterministic and reproducible microwave power and magnetic field strength at target location. We designed our waveguide to match the impedance (50Ω) of other electronics in the setup. Ignoring the local dielectric variation near the diamond membrane region, we designed the layout of the CPW based on the permittivity of the fused silica (3.7). The width of the center and the gap is set to 60 µm and 6 µm, respectively. To enhance the local field strength near the SnV region on the membrane, the center of the CPW is reduced to 6 µm. The ground lines of the waveguide is designed to across the membrane to compensate for the trench design, offering a balanced microwave delivering mode. We used a two-port microwave transmission design, demonstrating the potential of driving centers in multiple on-chip devices in the future. The two-port design also allows the microwave signal to be transmitted and dissipated outside of the chamber, relaxing the requirements for reflected signal management (such as circulator). The microscope image of the whole CPW design is shown in Figure S4 (a), with the transmission data of an identical device shown in Figure S4 (b). We show that the transmission loss is low from dc to 15 GHz, with the thermal loss ($P_{\text{in}} - P_{\text{out}} - P_{\text{reflected}}$) around the operation point (2.75 GHz) to be 1.5 dB.

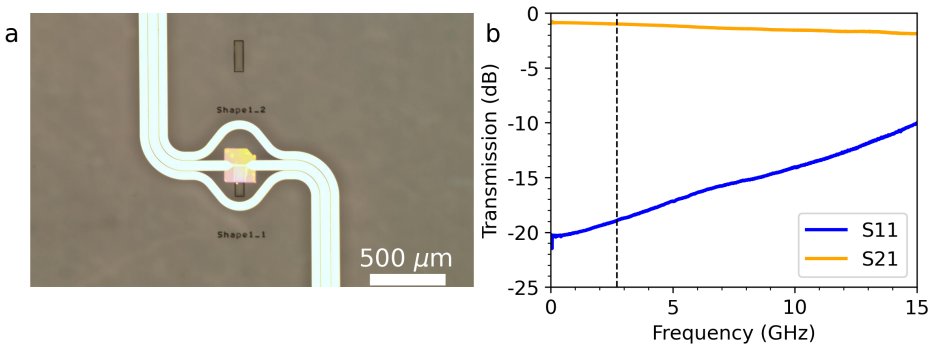

FIG. S4. Microwave CPW. (a) Microscope image of the CPW. The bonding pad for wire bonding is not shown. (b) The transmission of the CPW measured via a probe station using a vector network analyzer (VNA). The S11 is the reflection spectrum while the S21 is the transmission. The operation frequency (2.75 GHz) is labelled as a black, dashed line.

C. MW field simulation

We use COMSOL to simulate the magnetic field acting on nearby color centers. In the simulation, we set the microwave drive power to 24 dBm, the microwave drive frequency to 2.75 GHz, and set the characteristic impedance of the coplanar waveguide to 50 Ohm. The simulated structure and the magnetic field distribution are presented in fig:mwsimulation. Based on the simulation results, we expect the effective B field applied to the color centers ranges from 1 mT to 5 mT, corresponding to a transverse B field of 0.6 mT to 3 mT.

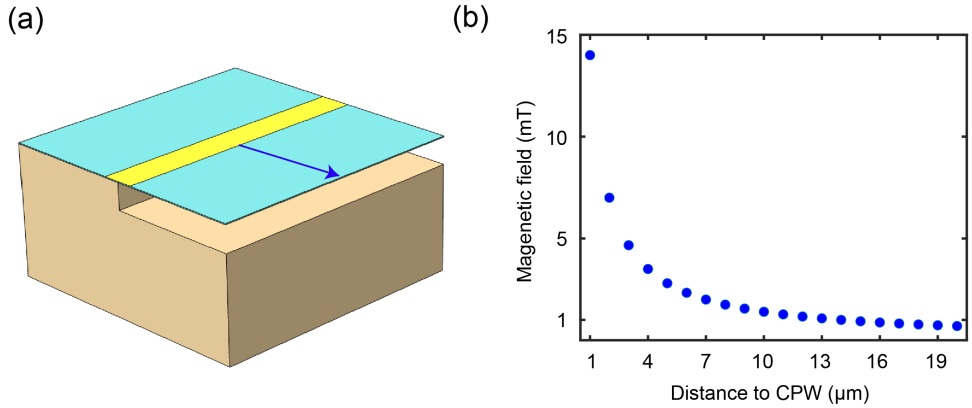

FIG. S5. Simulation of the microwave field in diamond membrane. (a) The 3D structure of the simulated device. The length (width) of the suspended diamond membrane is set to 50 µm (25 µm). (b) The magnetic field in diamond membrane, as a function of distance to the coplanar waveguide. The simulated depth is 40 nm from the top surface of diamond, and the simulated position is labeled as a blue arrow in (a).

D. Heating effect of the system

To investigate the power dependence of the SnV Rabi oscillation, we sweep the MW drive power and extract the Rabi frequency. We observe the expected $\sqrt{p}$-behaviour for low drive powers $p < 24$ dBm, but a clear deviation for larger drive powers. All the power and voltages are referred to the estimated value on the device, extracted by a separate calibration measurements in transmission geometry. We note that no increase in cryostat temperature is observed during the pulsed Rabi measurement.

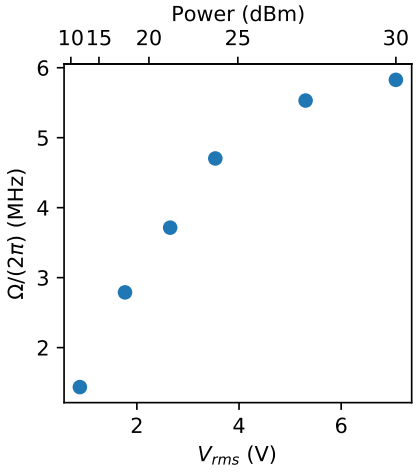

FIG. S6. Fitted Rabi-frequency $\Omega/2\pi$ over MW amplitude and power, showing the expected $\sqrt{p}$-behaviour for low drive powers $p < 24$ dBm.

The effect of heating on the emitter can be modeled as depicted in figure S7 (a) where we follow the approach taken in Ref [13]. The emitter is treated as a point-like object at a fixed distance X from the microwave line. Compared

to the SnV center the extent of the gold strip is well approximated as infinite such that we can model this as a 1D problem. Assuming the gold heats and cools instantaneously at the beginning and end of a microwave pulse, a solution to the 1D heat equation yields a temperature increase at the SnV center $\Delta T_{SnV} \propto erf\left(\frac{d}{\sqrt{4\alpha t}}\right)$ where α is the thermal diffusivity in diamond. Figure S7 (b) shows that the temperature at the emitter at asymptotically approaches the temperature of the microwave line. When higher Rabi frequencies are used another interesting effect is observed for more complex pulse sequences. Figure S7 (c) shows the effect of a sequence of pulses with a constant interpulse spacing τ_0. If τ_0 is significantly smaller than the time per pulse, the heat cannot flow away fast enough such that a net heating effect is observed per applied pulse. This means at high Rabi frequencies the coherence time of the spin can depend on the time between pulses.

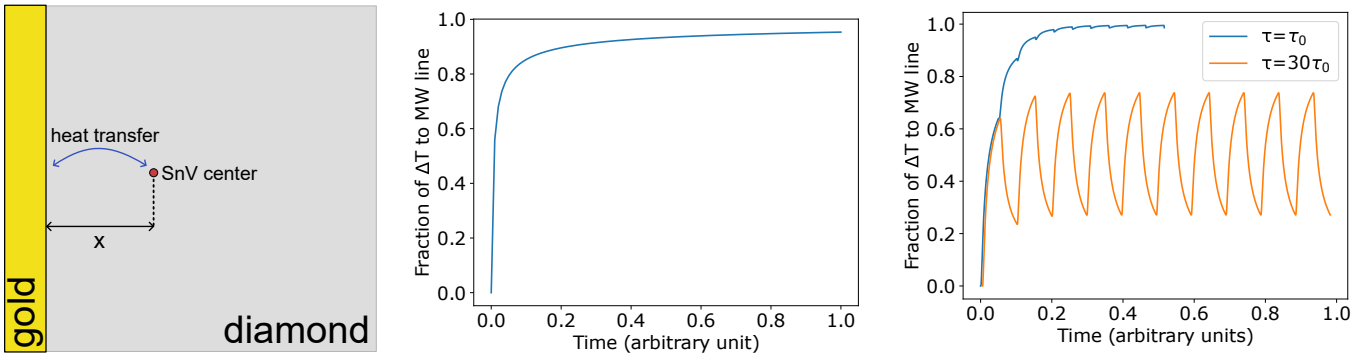

FIG. S7. (a) The SnV center as a point like object at a fixed distance x from the microwave gold transmission line. This is the model underlying the 1D heat equation solution. (b) Exemplary temperature increase vs time at the emitter position due to continuous microwave drive. The value is expressed as a fraction of the initial temperature difference approaching equilibrium. (c) Exemplary pulse sequence applying 10 successive microwave pulses each with intermediate spacing of τ_0 and $30\tau_0$, respectively. The maximum temperature differs significantly.

III. ADDITIONAL OPTICAL PROPERTIES OF THE STRAINED SNV

A. Polarization of the SnV

We probe the polarization of the strained SnVs by inserting a motor-mounted half-wave-plate and a linear polarizer in the detection path. The total intensity of the C-peak and the D-peak (named according to Ref. [1]) over polarisation angle are shown in Fig. S8. No magnetic field was applied. 0° in the graph indicates the magnet x-axis. The solid line is a fit of the expected polarisation, linear for the C-peak and circular for the D-peak, projected into the lab-frame according to the model in Ref. [1]. Both figures indicate a polarisation behaviour commensurate with bulk group IV color centers, showing that the polarisation is not changed when introducing strain.

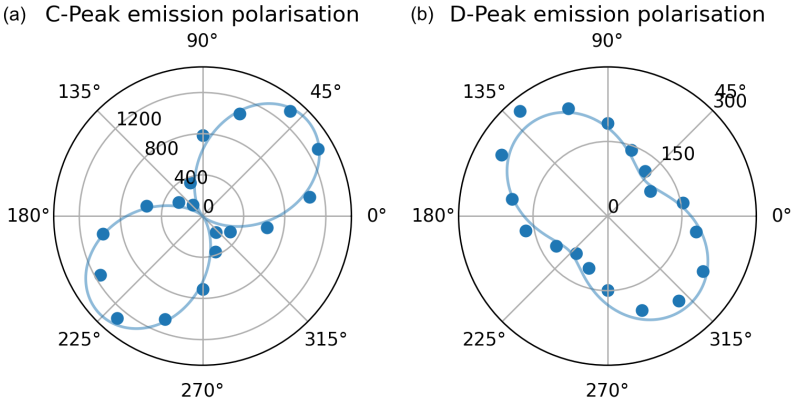

FIG. S8. Intensity of the (a) C-peak and (b) D-peak PL emission over linear polarisation in the lab-frame.

B. Optical lifetime

We extract the optical lifetime of the SnV by driving the C-transition at zero magnetic field with a single EOM-sideband and turning it off abruptly. The fall time is limited to 200 ps by the EOM. The decay time of the single-exponential is 4.933(190) ns which is similar to the bulk value, as shown in Fig. S9 [14]. An extended optical lifetime is expected for shallow-doped SnV centers due to the refractive index variation, which is in line with our observed value of the SnV center discussed in section 4.6. For this particular SnV center, the reduction of optical lifetime can be explained by the additional non-radiative decay channels on the diamond surface [15].

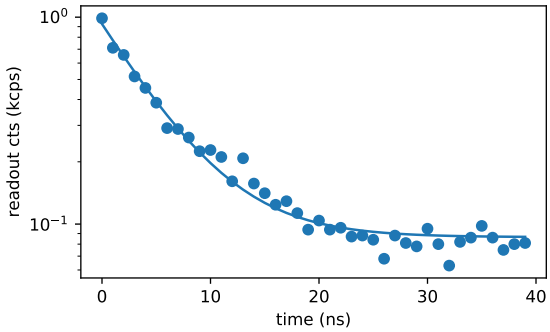

FIG. S9. Optical lifetime measurement of the C-transition. The solid line is a fit by a single-exponential, showing a decay time of 4.93(19) ns.

C. Power saturation

We extract the initialization rate, optical cyclicity and saturation power by prior knowledge of the optical lifetime and by sweeping the laser power [16]. The initialisation rates are fitted by $\frac{1}{\eta}\frac{\Gamma}{2}\frac{p/p_{\mathrm{sat}}}{1+p/p_{\mathrm{sat}}}$ and we extract a saturation power of 7.96 nW and an optical cyclicity of $\eta \approx 2018$. For the microwave spin control measurement we operate at a saturation parameter of $s = p/p_{\mathrm{sat}} \approx 10$ for the initialization and readout pulses.

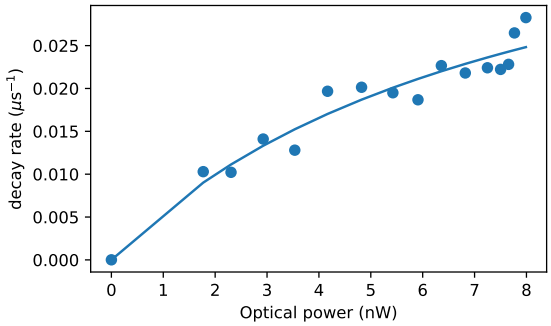

FIG. S10. Initialization rates for different laser powers with a fit by $\frac{1}{\eta}\frac{\Gamma}{2}\frac{p/p_{\mathrm{sat}}}{1+p/p_{\mathrm{sat}}}$

D. Long term stability of PLE

We acquire PLE for more than 11 hours to test the long-time stability of the SnV (see Fig. S11). We observe a very good frequency stability and only modest spectral wandering.

We fit each acquired PLE trace and extract the common mode shift of the spin-conserving transition [17] (Fig. S12 (a)). The Gaussian distribution of the shot-to-shot center frequencies has a standard deviation of σ =23.8(1) MHz. Similarly, the distribution of extracted spin-conserving splittings (Fig. S12 (b)) has a standard deviation of only σ =13.28(6) MHz.

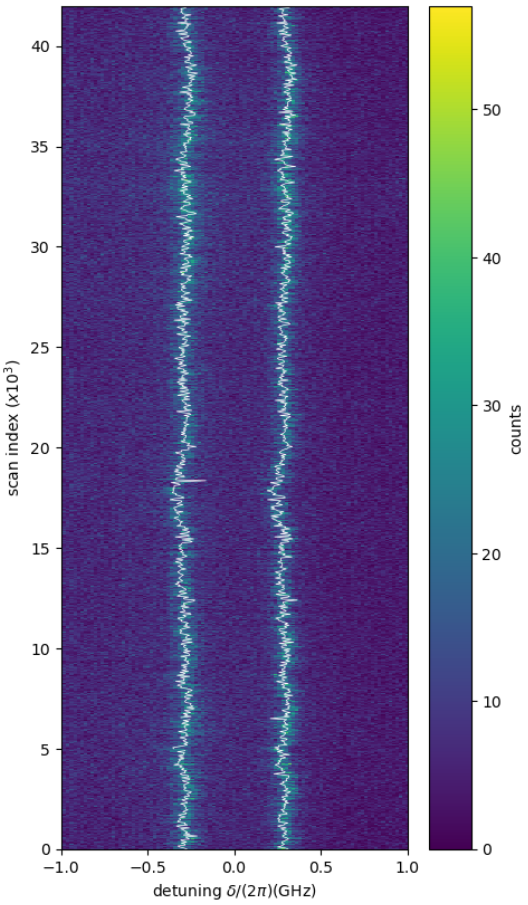

FIG. S11. Time evolution of the PLE line shape. Each vertical cut is the average of fast PLE scans over 1 s, with each shot of the measurement containing both green and red excitation. The solid white line is the fitted emitter resonance frequency.

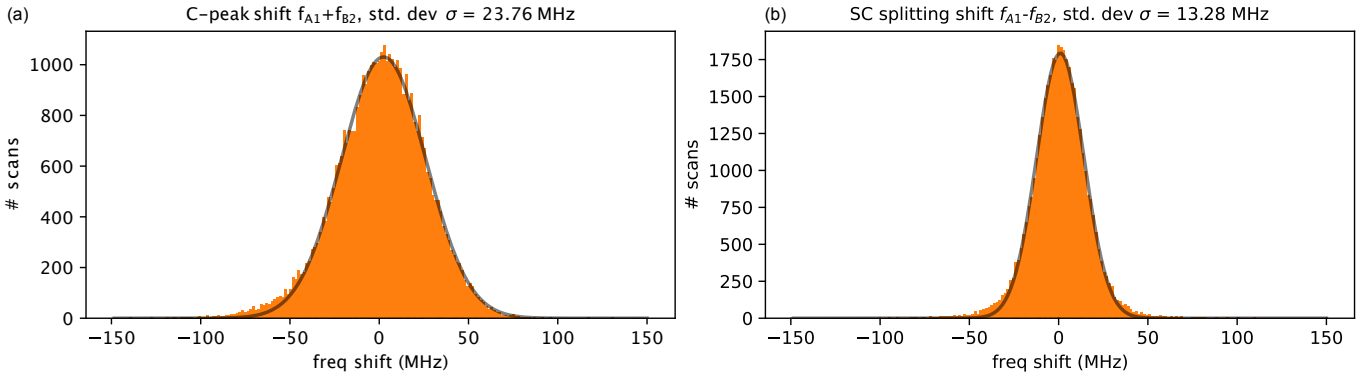

FIG. S12. (a) Histogram of the mean C-peak frequency from shot-to-shot. (b) Histogram of the spin-conserving splitting from shot-to-shot. The grey line is a fit with a Gaussian distribution.

IV. OPTICAL CONTROL OF THE SNV SPIN

A. Optical splitting with external B field

We scan the magnetic field over the whole sphere at fixed magnitude. The path between the approximately equidistant points is numerically minimised. The hysteresis of the B-field is on the order of 10 % as estimated from linear sweeps along a single magnet axis.

The splitting of the $A1, B2$ optical transitions with varying B fields can be computed by diagonalizing the system Hamiltonian H_{sys} of Eq. 1, and the results are shown in Fig S13 (b) and (c). When constructing the Hamiltonian, we considered the Steven's term g_L in the reduction factor q as a free parameter. The Steven's term, as discussed in subsection I A 3, originates from the defect symmetry being lower than $O(3)$. Here we determined the range of g_L by matching the experiments. We plot the difference of the splitting when the B field is aligned with the defect quantization axis ($\theta_B = 0$), and aligned along the equator ($\theta_B = \pi/2$) with varying $g_L \in [0, 1]$ in Fig S13 (c). The white region in the plot (values close to zero) corresponds to the two splittings being close in energy, matching the experimental observations. Therefore our calculations enabled the narrowing down of the the possible values of Steven's factor to $g_{L,\text{gs}} \in [0.5, 1.0]$ and $g_{L,\text{es}} \sim 2g_{L,\text{gs}} - 1$.

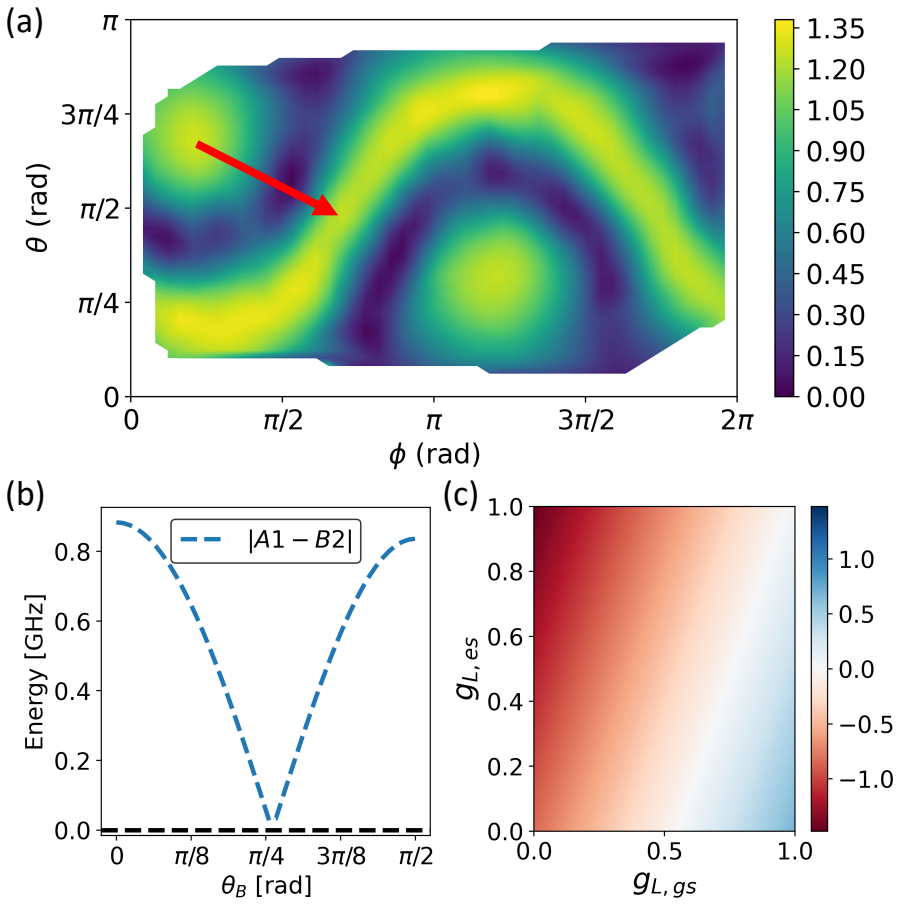

FIG. S13. Experimental measured and simulations of the spin-conserving optical transitions $A1, B2$ with varying external magnetic field B. (a) Scanning of the splittings of $A1, B2$ transitions with varying B field directions. The magnitude of B is set to 0.2 T. The x, y axis represents the azimuthal (ϕ) and polar angle (θ) of the B field in the Lab frame. The two poles on the plot represent directions along the quantization axis of the SnV^- and the belt represents the equator. (b) Simulated splittings of the $A1, B2$ transitions by diagonalizing the system Hamiltonian along a chosen path of varying B fields, where the path is depicted as a red arrow in (a). The x axis represents the polar angle of the B field in the defect frame. Simulation agrees qualitatively with experiments with the magnitude of splitting underestimated by 0.4 GHz. (c) The differences between the $A1, B2$ splittings at $\theta_B = 0$ and $\theta_B = \pi/2$ with varying Steven's reduction factor. The white region corresponds to pairs of Steven's reduction factor for ground and excited states, when taken into the diagonalized Hamiltonian, that match the experimental observations.

B. Optical cyclicity of the SnV

We coarsely align the B-field by matching it to the polarisation of the optical dipoles (see SI section 3.1) and obtain an optical cyclicity of $\eta \approx 2018$. The cyclicity has a single local maximum close to the pole of the emitter axis, such that we can increase it by sweeping two of the three magnet axes independently. We extract the cyclicity by measuring the decay rate of one of the spin-conserving transitions. The frequency of the sidebands driving the transitions is fixed, noting that the change in B-field magnitude corresponds to a change in spin-conserving splitting within one optical linewidth. One can see only a modest increase in cyclicity in Fig. S14 (a) and (b), such that we conclude that strain limits the maximum achievable cyclicity. Nevertheless, the error introduced by the finite cyclicity will be negligible in spin-photon entanglement protocols due to the relatively high value and enable single-shot readout with nanostructures or microcavities.

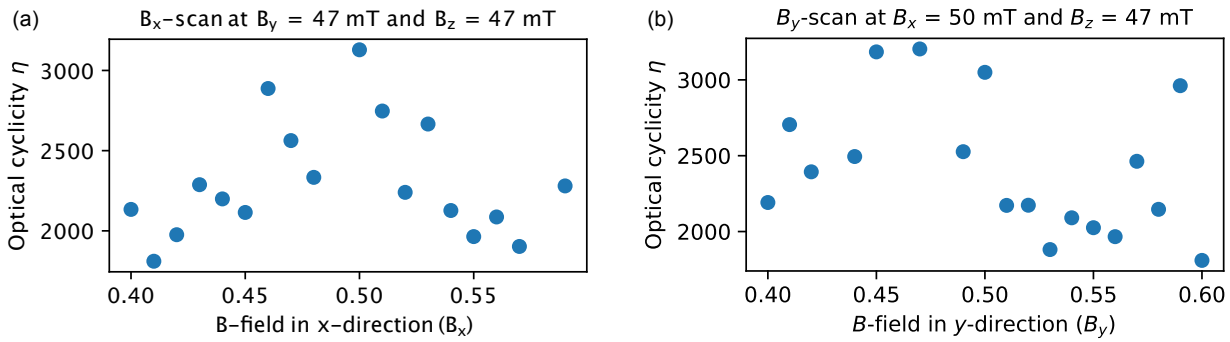

FIG. S14. Optical cyclicity at (a) fixed B_y and B_z, with swept B_x and (b) fixed B_x and B_z, with swept B_y.

The optical cyclicity, as a branching ratio between spin-conserving and spin-flipping transitions, depends on both system properties and the external optical field. Theoretically, we can only investigate the system property side. Here we investigate an alternative problem—spontaneous emission rate ratio between spin-conserving and spin-flipping transitions—optical cyclicity with absence of the external optical excitation.

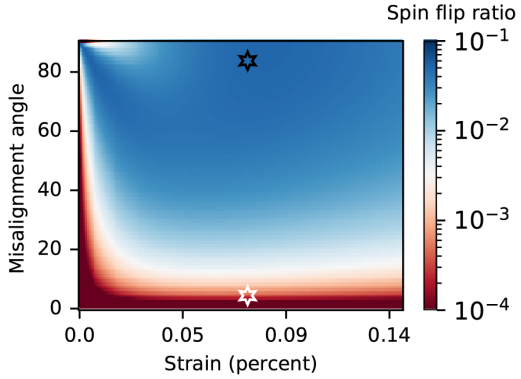

FIG. S15. The calculated cyclicity of the SnV with respect to the B field polar angle θ and the strain magnitude. The operation point of the MW-based (all-optical) control of the SnV spin qubit is highlighted in white (black) stars.

According to Ref [1], we use optical dipole matrices to calculate the emission rate of the two transitions. The rate (probablity) can be expressed using Fermi's Golden Rule:

$$P = 2\pi\rho |\langle\psi_f| |e \cdot \hat{\mathbf{r}}| |\psi_i\rangle|^2 = 2\pi\rho |\langle\psi_f| |\hat{\mathbf{p}}| |\psi_i\rangle|^2 \tag{14}$$

Where ρ is the density of states where we set to 1, the $|\psi_f\rangle$ and $|\psi_i\rangle$ are the final and initial state of the SnV which we assign to the excited state minimum $|e_A \downarrow\rangle$ and ground states $|e_1 \downarrow\rangle$ ($|e_2 \uparrow\rangle$) for spin conserving (flipping) transitions. The transition probablity (rate) P is related to the optical dipole $\hat{\mathbf{p}}$ which is defined as:

$$\hat{p_x} = e\begin{bmatrix}1&0&0&0\\0&1&0&0\\0&0&-1&0\\0&0&0&-1\end{bmatrix}, \hat{p_y} = e\begin{bmatrix}0&0&-1&0\\0&0&0&-1\\-1&0&0&0\\0&-1&0&0\end{bmatrix}, \hat{p_z} = e\begin{bmatrix}1&0&0&0\\0&1&0&0\\0&0&1&0\\0&0&0&1\end{bmatrix} \tag{15}$$

Using the above definition, we can calculate the spin flip ratio which is the inverse of spontaneous cyclicity $\frac{1}{\eta} = \frac{P_{\text{flipping}}}{P_{\text{conserving}}}$ with respect to the strain magnitude and the B field polar angle θ, as shown in Figure S15. The operation point of the MW-based (all-optical) control of the SnV spin qubit is highlighted in white (black) stars, showing a cyclicity of $\geq$2000 if $\theta < 4°$ and a cyclicity of $\approx$20 if $\theta > 85°$, in a rough agreement with the experimentally observed values. We note that the presence of the moderate-level strain will make the overall cyclicity lower than the strain-free case, but the achievable value is still compatible with single shot readout requirements if the signal count can be improved by device design or setup optimization.

C. All-optical spin control and operation at perpendicular B-fields

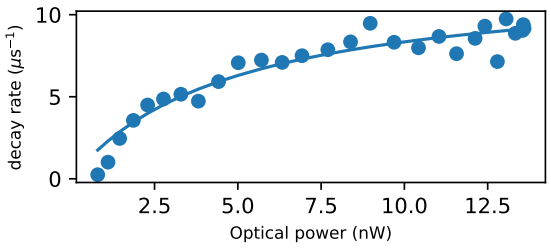

FIG. S16. Initialization rates for different laser powers with a fit by $\frac{1}{\eta}\frac{\Gamma}{2}\frac{p/p_{\text{sat}}}{1+p/p_{\text{sat}}}$

We implemented the all-optical control technique shown in Ref. [16] on Device 1 on a strained SnV with a ground state splitting of Δ_{GS} =1384 GHz. We extracted an optical lifetime of 7.04(10) ns which is compatible for an SnV in proximity of a surface [15]. We set the magnetic field to $|B| = 100$ mT perpendicular to the emitter axis. From the saturation power measurement in Fig. S16 we extract a saturation power of p_{sat} =4.82(81) nW and a cyclicity of $\eta = 5.78(36)$ The low saturation power and low cyclicity indicate that efficient all-optical control should be possible in principle.

We implement an optical lambda system on the spin-conserving transition A1 and spin-flipping transition A2 and measure coherent population trapping (CPT) by driving both transitions simultaneously (Fig. S17). Fitting the data with the model in Ref. [16, 18], we get an excited state decay rate of $\Gamma/2\pi$ =26.52(91) MHz, only a factor of 1.17 larger than the transform-limited linewidth $\Gamma_0/(2\pi) = 22.60(5)$ MHz.

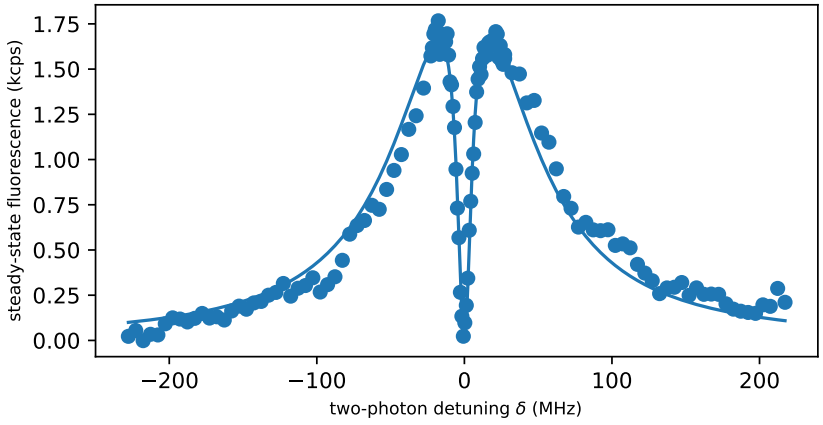

FIG. S17. Coherent population trapping measured on an SnV at perpendicular magnetic fields.

For all-optical Raman control, we choose to operate at a single-photon detuning of $\Delta = 1.5$ GHz. At the lowest laser sideband powers of $p = 455$ nW, we get an intrinsic ODMR linewidth of $\delta f = 1/T_{2*} = 899(54)$ kHz (Fig. S18). The qubit frequency of $f_{\mathrm{qubit}} = 2.321$ GHz, yields a g-factor of $g = 0.83$, meaning that perpendicular fields can couple to the SnV efficiently due to strain.

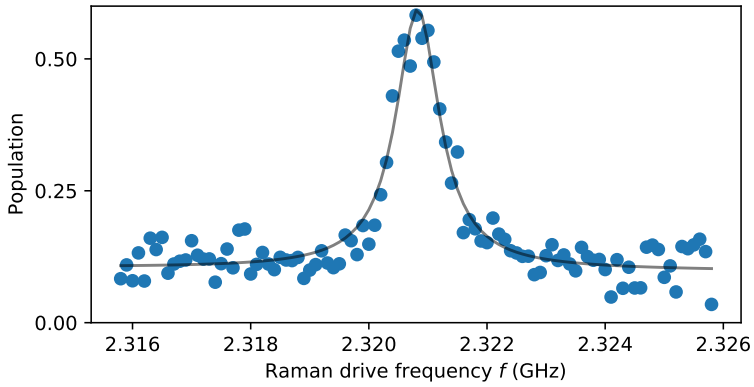

FIG. S18. All-optical pulsed ODMR at perpendicular B-field directions.

We sweep the Raman drive time T at laser sideband powers of $p = 1012$ nW and extract a Rabi frequency of $\Omega/2\pi = 450(47)$ kHz(Fig. S19) and a π-gate fidelity of $F_\pi = 83(2)$ %, similar to Ref. [16].

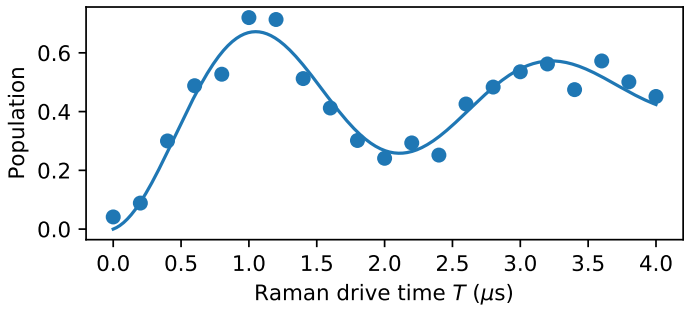

FIG. S19. All-optical spin control at perpendicular B-field directions and sideband power of $p = 1012$ nW.

Ramsey measurements (Fig. S20) yield an inhomogeneous dephasing time of $T_{2*} = 1.13(7)$ µs and a Hahn-Echo measurements (Fig. S21) a dephasing time of $T_2 = 35.5(30)$ µs.

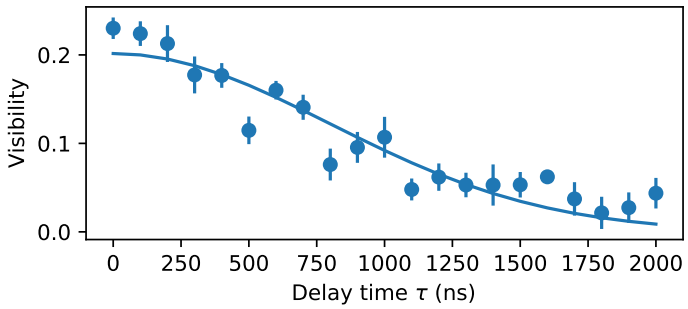

FIG. S20. All-optical Ramsey measurement showing an inhomogeneous dephasing time of $T_{2*} = 1.13 \pm 0.07$ µs

We additionally measured the spin decay time T_1 at the perpendicular field orientation and found much shorter times on the order of 100 µs (Fig. S22).

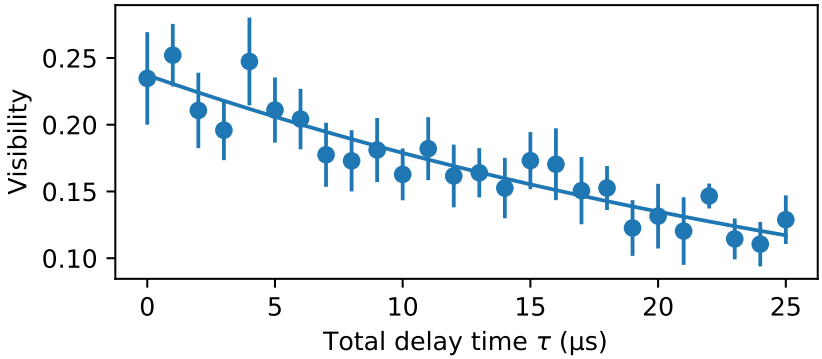

FIG. S21. All-optical Hahn-Echo measurement showing a dephasing time of $T_2 = 35.45 \pm 2.96$ μs

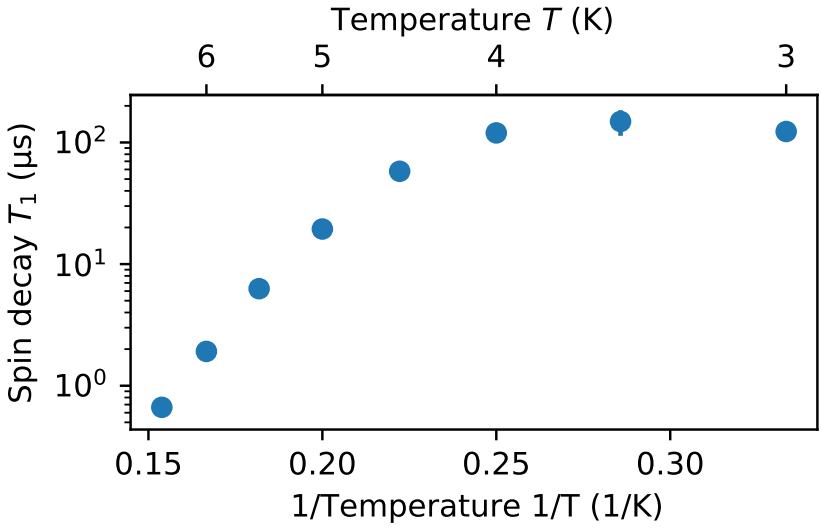

FIG. S22. Spin decay T_1 over inverse temperature $1/T$.

D. Spin T_1 analysis

Phonon-induced depolarization of group IV centers' spin is the dominant source of decoherence. Therefore, improving the spin decay time T_1 is the central task to enhance the coherence of the system. As discussed in Ref. [11], the spin decay time T_1 in the group IV has two meanings, the orbital relaxation time T_1^{orbit} between the energy levels in different orbital branches but with same spin projection, and the T_1^{spin} between the qubit levels with frequency ω_s. Ultimately, the T_1^{spin} is the factor that directly relates to the coherence of the SnV, so we limit our T_1 discussion to T_1^{spin} only.

There are three phonon-induced T_1^{spin} decay path [11], including direct single phonon, resonant two phonon (Orbach process) [19], and off-resonant two phonon (Raman process). Similar to SiV, the SnV shows much slower single phonon and Raman spin decay, so we focus on the Orbach process and study its dependence with the B field orientation (θ) and the strain magnitude. Adapted from Ref. [19], we write the decay rate γ_{spin}^2 as follows:

$$\gamma_{spin}^2 \propto \frac{\Delta_{gs}^3}{\exp\{(h\Delta_{gs}/k_BT)\} - 1} \frac{\left|\sum \langle e_1 \downarrow| H_\epsilon^{AC} |e_j\rangle \langle e_j| H_\epsilon^{AC} |e_2 \uparrow\rangle\right|^2}{\sum |\langle e_i| H_\epsilon^{ac} |e_j\rangle|^2} \tag{16}$$

where i represent the states of the lower orbital branch ($|e_1 \downarrow\rangle$, $|e_2 \uparrow\rangle$) and j represent the states of the upper orbital branch ($|e_3 \downarrow\rangle$, $|e_4 \uparrow\rangle$). The H_ϵ^{ac} denotes an AC strain field which correlates to the phonon interaction in the crystal.

We used balanced magnitude for the $H^{AC}_{\epsilon_{Ex}}$ and $H^{AC}_{\epsilon_{Ey}}$ by setting the H^{ac}_{ϵ} as follows:

$$H^{ac}_{\epsilon} = e \begin{bmatrix} -1 & 0 & 1 & 0 \\ 0 & -1 & 0 & 1 \\ 1 & 0 & 1 & 0 \\ 0 & 1 & 0 & 1 \end{bmatrix}, \tag{17}$$

The relative decay rate at temperature 4 K with the maximum normalized to 1 is shown in Figure S23, with MW-based (small θ) and all-optical (large θ) operation points for spin control of the SnV highlighted in black (white) stars. We observe a ratio of 500 to 1200 between the two T_1^{spin}, which is roughly inline with our experimental values measured at 6 K (MW-based control T_1^{spin} =2.5 ms, all-optical control T_1^{spin} =1.65 µs). We note that as a pre-factor, the temperature would not change the decay rate ratio between the two configurations. This ratio reiterates the fact that the Orbach process is the dominant factor for the T_1^{spin} decay.

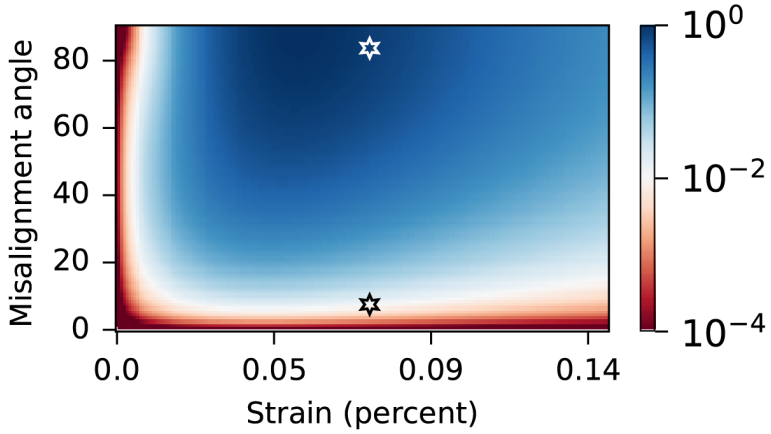

FIG. S23. The calculated Orbach decay rate of the SnV with respect to the B field polar angle θ and the strain magnitude. The operation point of the MW-based (all-optical) control of the SnV spin qubit is highlighted in black (white) stars.

V. MW CONTROL OF THE SNV SPIN

A. Randomized benchmarking

The gates are chosen from the Clifford group and are $\{I, \pi_x, \pi_y, \pi_x/2, -\pi_x/2, \pi_y/2, -\pi_y/2\}$. We randomly choose $(N-1)$-gates and use the last gate to undo the sequence, followed by a z-basis measurement. The last gate is part of the Clifford group. We get the π-gate from Rabi measurements and adjust the time t_π accordingly. The identity is implemented as wait-time for t_π, whereas $\pi/2$-gates have a duration of $t_{\pi/2}$. No buffer times are used which would make the qubit prone to dephasing errors, but the drive amplitude is reduced such that local heating effects is not a limiting factor. All randomized benchmarking measurements were taken at a Rabi frequency of $\Omega/(2\pi) = 2.8$ MHz. A total of 10 randomized sequences were applied each time to average out over different implementations. The fidelity F is extracted by fitting the readout with $A * F^N + B$, from which we get the error per Clifford gate [20].

B. Ramsey T_{2*} at different qubit frequency

We change the applied magnetic field magnitude from 81.5 to 117 mT and measure the Ramsey dephasing time T_2^*. We extract $T_2^* = 2.63(14)$ µs at the qubit frequency of 3.694 GHz (see Fig. S24), indicating that g-factor fluctuations as reported in Ref.[21] are not limiting the observed T_2^*.

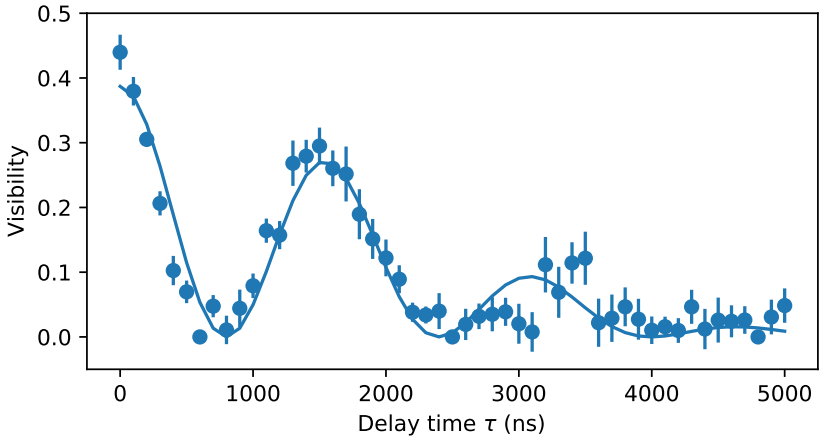

FIG. S24. Ramsey measurement of the inhomogeneous dephasing time T_2^* at a qubit frequency of 3.694 GHz.

C. Ramsey measurements with phase-readout

Fig. S25 shows the measurement from which we extract T_{2*} Ramsey and the modulation of the qubit frequency in Fig. 4 (a) in the main text. We fit for every time delay a modulation of the phase by $A * \cos\phi + B$, where A is the visibility shown in the main text and B is the mean value for all time delays averaged over all phases. We then extract the inhomogenous dephasing time T_{2*} by fitting A over delay time τ with an Gaussian envelope $\propto \exp\{((-\tau/T_{2*})^2)\}$. With this technique, we can distinguish with certainty a real modulation of the qubit frequency (loss in coherence and visibility) versus a detuning error (no total loss of visibility, but no readout at certain delays and phases). The origin of the beating pattern needs further investigation. The MW-electronics were tested for any modulation. Likely candidates could be surface spins or substitutional nitrogen centres (P1-centres) with a large gyromagnetic ratio close to the one of a free electron ($g = 2$) resulting in relatively large couplings even at large distances.

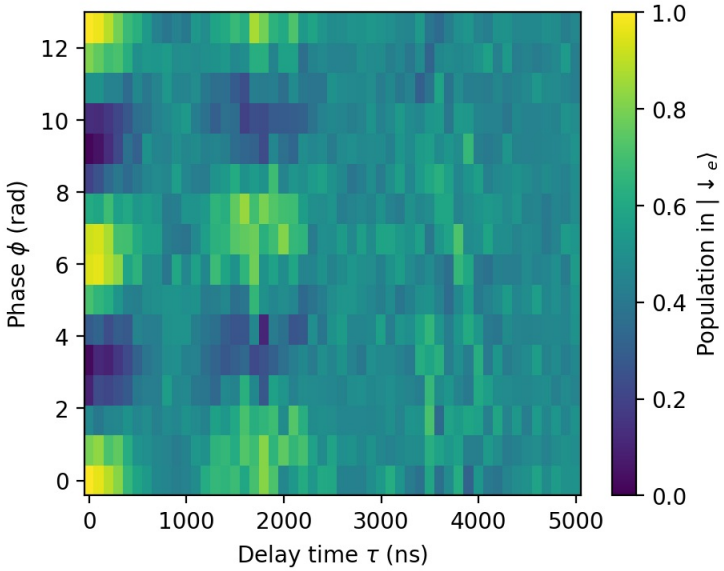

FIG. S25. Ramsey measurement of T_2^*. Both the delay-time τ and the phase of the second $\pi/2$-pulse are varied.

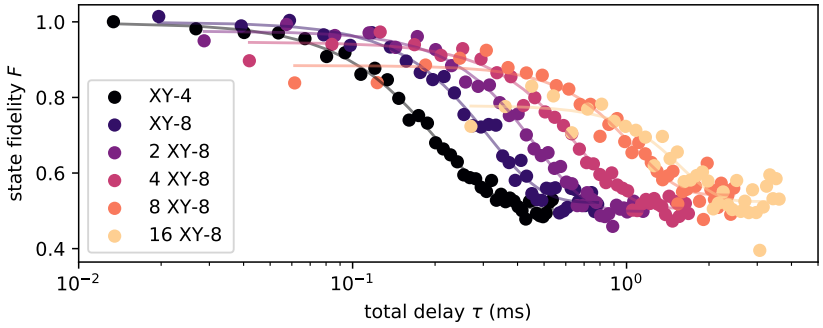

FIG. S26. State fidelity F over total delay time τ for XY-pulse sequences.

D. XY-sequences

Fig. S26 shows the coherence over total time delay τ in the XY-family of dynamical-decoupling sequences. We observe an almost identical scaling of coherence time over the number of π-pulses (see main text Fig. 4 c). Because of the much smaller sensitivity of XY- pulse sequences with regards to rotation- or offset errors compared to CPMG sequences, we conclude that our control does not limit the coherence [22].

VI. EXPERIMENTAL DETAILS

A. Device fabrication

The diamond membrane substrate was generated via He^+ implantation and annealing. 450 nm-thick diamond overgrowth layer was introduced in a diamond chemical vapor deposition (CVD) chamber, followed by a ^{120}Sn implantation with $2 \times 10^8\,\mathrm{cm}^{-2}$ dose and 40 nm target depth. Individual membranes were patterned via lithography and electrochemically etched to undercut the graphitized layer. The target membrane was then transferred to a HSQ-coated fused silica substrate with a 5 µm-deep etched trench to the generate suspended area. The substrate was annealed at 600 °C for 8 h in argon atmosphere. Membrane was thinned down to 160 nm via ICP RIE etching using Ar/Cl_2, O_2/Cl_2, and O_2 recipes. The microwave coplanar waveguide was lithographically defined, followed by Ti and Au deposition with thicknesses of 10 nm and 200 nm, respectively. Excess resist was lift-off using 80 °C NMP solutions.

B. Measurement setup

All the measurement data in this work were taken in Cambridge, UK. The device was studied in a closed-cycle cryostat (attoDRY 2100) with a base temperature of 1.7 K at the device and in which the temperature can be tuned with a resistive heater located under the sample mount. Superconducting coils around the sample space allow the application of a vertical magnetic field from 0 to 9 T and a horizontal magnetic field from 0 to 1 T. Unless explicitly stated otherwise, all measurements were conducted at $T = 1.7$ K. The optical part of the set-up consists of a confocal microscope mounted on top of the cryostat and a microscope objective with numerical aperture 0.82 inside the cryostat. The device is moved with respect to the objective utilizing piezoelectric stages (ANPx101/LT and ANPz101/LT) on top of which the device is mounted. Resonant excitation around 619 nm is performed by a second harmonic generation stage (ADVR RSH-T0619-P13FSAL0) consisting of a frequency doubler crystal pumped by a 1238 nm diode laser (Sacher Lasertechnik Lynx TEC 150). The frequency is continuously stabilized through feedback from a wavemeter (High Finesse WS/7). The charge environment of the SnV- is reset with microsecond pulses at 532 nm (Roithner LaserTechnik CW532-100). PL measurements were done with a Teledyne Princeton Instruments PyLoN:400BR eXcelon CCD and SpectraPro HRS-750-SS Spectrograph. Optical pulses are generated with an acousto-optic modulator (Gooch and Housego 3080-15 in the 532 nm path and AA Opto Electronics MT350-A0,2-VIS) controlled by a delay generator (Stanford Research Instruments DG645). For resonant excitation measurements, a long-pass filter at 630 nm (Semrock BLP01-633R-25) is used to separate the fluorescence from the phonon-sideband from the laser light. The fluorescence is then sent to a single photon counting module (PerkinElmer SPCM-AQRH-16-FC), which generates TTL pulses sent to a time-to-digital converter (Swabian Timetagger20) triggered by an arbitrary waveform generator (Tektronix

AWG70002A). Photon counts during "initialize" and "readout" pulses are histogrammed in the time-tagger to measure the spin-population. Sidebands driving both resonantly transitions as well as off-resonant all-optical control were generated by an amplitude electro-optic modulator (Jenoptik AM635), and the amplitude, phase, and frequency of the sidebands are controlled by a 25 Gs/sec arbitrary waveform generator (Tektronix AWG70002A). The EOM is locked to its interferometric minimum with a lock-in amplifier and PID (Red Pitaya, STEMlab 125-14) and using a freely available Lock-in+PID application [23] with a feedback loop on the signal generated by a photodetector (Thorlabs PDA100A2).

Microwave pulses are generated with the second channel of the arbitrary waveform generator and amplified with a low-noise amplifier (Minicircuits ZX60-83LN12+) and a high-power amplifier (Minicircuits ZVE-3W-83+). Microwave signals inside the cryostat are delivered via the in-built pico-coax cables, self-soldered cables and a customised PCB. The signal is transmitted through a second line and terminated outside of the cryostat with 50 Ohms.

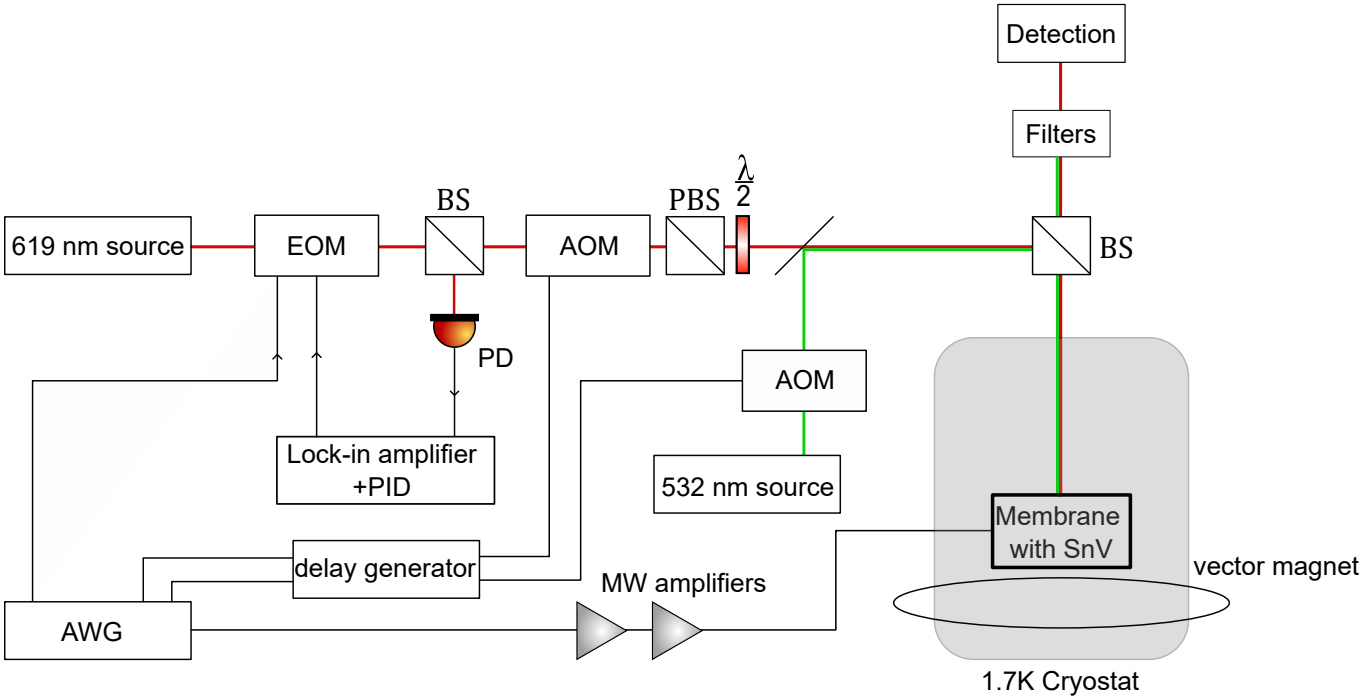

FIG. S27. Sketch of the experimental set-up described in detail in the text.

[1] C. Hepp, *et al.*, *Physical Review Letters* **112** (2014).
[2] G. Thiering, A. Gali, *Physical Review X* **8**, 021063 (2018).
[3] J. P. Perdew, K. Burke, M. Ernzerhof, *Physical Review Letters* **77**, 3865 (1996).
[4] J. Sun, A. Ruzsinszky, J. P. Perdew, *Physical Review Letters* **115**, 036402 (2015).
[5] T. Hahn, R. Kirby, *AIP Conference Proceedings* (American Institute of Physics, 1972), vol. 3, pp. 13–24.
[6] N. OIKAWA, A. MAESONO, R. TYE, *THERMAL CONDUCTIVITY* **24**, 405 (1999).
[7] R. R. Reeber, K. Wang, *Journal of Electronic Materials* **25**, 63 (1996).
[8] H. McSkimin, P. Andreatch Jr, *Journal of Applied Physics* **43**, 2944 (1972).
[9] Y. Siew, *et al.*, *Journal of The Electrochemical Society* **147**, 335 (2000).
[10] N. Sheng, C. Vorwerk, M. Govoni, G. Galli, *Journal of Chemical Theory and Computation* **18**, 3512 (2022).
[11] S. Meesala, *et al.*, *Physical Review B* **97**, 205444 (2018).
[12] N. D. Lai, D. Zheng, F. Jelezko, F. Treussart, J.-F. Roch, *Applied Physics Letters* **95** (2009).
[13] C. T. Nguyen, *et al.*, *Phys. Rev. B* **100**, 165428 (2019).
[14] M. E. Trusheim, *et al.*, *Physical Review Letters* **124**, 023602 (2020).
[15] J. Görlitz, *et al.*, *New Journal of Physics* **22**, 0 (2020).
[16] R. Debroux, *et al.*, *Physical Review X* **11** (2021).
[17] J. Arjona Martínez, *et al.*, *Phys. Rev. Lett.* **129**, 173603 (2022).
[18] M. Fleischhauer, A. Imamoglu, J. P. Marangos, *Reviews of modern physics* **77**, 633 (2005).

[19] R. Orbach, *Proceedings of the Royal Society of London. Series A, Mathematical and Physical Sciences* **264**, 458 (1961).
[20] E. Knill, *et al.*, *Physical Review A* **77**, 012307 (2008).
[21] D. D. Sukachev, *et al.*, *Physical Review Letters* **119** (2017).
[22] A. M. Souza, G. A. Álvarez, D. Suter, *Philosophical Transactions of the Royal Society A: Mathematical, Physical and Engineering Sciences* **370**, 4748 (2012).
[23] M. A. Luda, M. Drechsler, C. T. Schmiegelow, J. Codnia, *Review of Scientific Instruments* **90**, 023106 (2019).